ADVANCED ELECTRONIC MATERIALS
Open Access
www.advelectronicmat.de

Non-Destructive X-Ray Imaging of Patterned Delta-Layer Devices in Silicon

Nicolò D'Anna, Dario Ferreira Sanchez, Guy Matmon, Jamie Bragg, Procopios C. Constantinou, Taylor J.Z. Stock, Sarah Fearn, Steven R. Schofield, Neil J. Curson, Marek Bartkowiak, Y. Soh, Daniel Grolimund, Simon Gerber, and Gabriel Aeppli*

The progress of miniaturization in integrated electronics has led to atomic and nanometer-sized dopant devices in silicon. Such structures can be fabricated routinely by hydrogen resist lithography, using various dopants such as P and As. However, the ability to non-destructively obtain atomic-species-specific images of the final structure, which would be an indispensable tool for building more complex nano-scale devices, such as quantum co-processors, remains an unresolved challenge. Here, X-ray fluorescence is exploited to create an element-specific image of As dopants in Si, with dopant densities in absolute units and a resolution limited by the beam focal size (here ≈1 μm), without affecting the device's low temperature electronic properties. The As densities provided by the X-ray data are compared to those derived from Hall effect measurements as well as the standard non-repeatable, scanning tunneling microscopy and secondary ion mass spectroscopy, techniques. Before and after the X-ray experiments, we also measured the magneto-conductance, which is dominated by weak localization, a quantum interference effect extremely sensitive to sample dimensions and disorder. Notwithstanding the 1.5×10^{10} Sv (1.5×10^{16} Rad cm^{-2}) exposure of the device to X-rays, all transport data are unchanged to within experimental errors, corresponding to upper bounds of 0.2 Angstroms for the radiation-induced motion of the typical As atom and 3% for the loss of activated, carrier-contributing dopants. With next generation synchrotron radiation sources and more advanced optics, the authors foresee that it will be possible to obtain X-ray images of single dopant atoms within resolved radii of 5 nm.

1. Introduction

The ability to build nanometer-scale dopant structures buried in Si has led to great progress in classical and quantum technologies.[1] As the patterned structures become increasingly small and complex, it becomes indispensable to develop techniques to non-destructively image the dopant structures for device inspection and quality control.[2–4]

Scanning tunneling microscopy (STM) can be used to pattern acceptors and donors into Si with atomic resolution using hydrogen resist lithography.[5,6] The technique has created complementary metal-oxide-semiconductor compatible structures, including 2D conductive sheets,[7] 3D structures,[8] nano-wires,[9] and quantum dots.[10] Precisely measuring the location of buried dopants patterned by STM is challenging and can only be accomplished with STM itself for patterns extremely near to the surface.[11,12] Techniques capable of imaging such nano-scale structures such as secondary-ion mass spectrometry (SIMS)[13] and atom

N. D'Anna, D. Ferreira Sanchez, G. Matmon, P. C. Constantinou, M. Bartkowiak, Y. Soh, D. Grolimund, S. Gerber, G. Aeppli
Paul Scherrer Institut
Villigen 5232, Switzerland
E-mail: gabriel.aeppli@psi.ch, ndanna@ucsd.edu
N. D'Anna, G. Aeppli
Department of Physics and Quantum Center
Eidgenössische Technische Hochschule Zürich
Zürich CH-8093, Switzerland

The ORCID identification number(s) for the author(s) of this article can be found under https://doi.org/10.1002/aelm.202201212.

DOI: 10.1002/aelm.202201212

J. Bragg, P. C. Constantinou, T. J.Z. Stock, S. Fearn, S. R. Schofield, N. J. Curson
London Centre for Nanotechnology
University College London
London WC1H 0AH, UK
J. Bragg, N. J. Curson
Department of Electronic and Electrical Engineering
University College London
London WC1H 0AH, UK
P. C. Constantinou, S. R. Schofield
Department of Physics and Astronomy
University College London
London WC1E 6BT, UK
S. Fearn
Department of Materials
Imperial College of London
London SW7 2AZ, UK
G. Aeppli
Institute of Physics
Ecole Polytechnique Fédérale de Lausanne (EPFL)
Lausanne 1015, Switzerland

probe tomography,[14] are typically destructive, making them unsuitable for device quality control.[15] Two techniques that can image the dopants non-destructively are broadband electrostatic force microscopy (bb-EFM)[16] and infrared ellipsometry,[17] however both come with limitations. In particular, bb-EFM can only measure the polarity of the dopant and not its elemental species, whereas infrared ellipsometry can, in principle, obtain information regarding the species and density of atoms, but it is model-dependent and requires elaborate fits to the data.

Here we show that X-ray fluorescence (XRF) can be used to create non-destructive atomic-species-specific images of dopants in Si with a resolution only limited by the beam-size, in our case of order one micron. This technique uses synchrotron X-rays to locally ionize the atoms in the investigated device, leading to the emission of photons via fluorescence. The measurements are conducted at ambient temperature and pressure, and the photon spectrum is analyzed to obtain the species and densities of the atoms in the device. Low-temperature magneto-transport of the 2D Hall-bar device before and after imaging with the X-ray fluorescence demonstrates that the technique does not alter the electrical characteristics of the device, namely the free carrier density, electron mean free path, coherence length, and vertical confinement. We conclude therefore that the technique is non-destructive. As an extension of the principle demonstrated here, by rotating the sample in the X-ray beam it will be straightforward to obtain a tomographical 3D reconstruction of the atoms' positions in the device.[4,18,19]

2. X-Ray Fluorescence

When an X-ray photon impinges on an atom it can be absorbed by the atom that will, in turn, be ionized. Inner orbital electrons are expelled from the atom and replaced by outer orbital electrons. In this process photons are emitted with wavelengths corresponding exactly to the energy difference between the electrons' orbitals. Therefore, the resulting energy spectrum of the fluorescence photons will uniquely identify the atomic species of the ionized atom. In the presence of many different atoms the fluorescence spectrum will be the sum of the different spectral lines. As each atomic spectrum is well-known, it is straightforward to decompose an arbitrary fluorescence spectrum into element-specific components.[20]

XRF experiments reported here were conducted at the microXAS beamline of the Swiss Light Source synchrotron.[21] The beamline employs high brightness X-rays in the energy range from ≈4 to 22 keV. At the photon energy of 11.88 keV used here, the delivered photon flux is approximately $I_0 = 10^{10}$ photons s^{-1} when the beam is focused to 1×1 μm^2 using a Kirkpatrick–Baez mirror system, and an energy resolution of $\Delta E/E < 10^{-4}$ is chosen. The beam was set to normal incidence. An X-ray energy of 11.88 keV is sufficiently high to dislodge core electrons from the As *K*-levels, without exciting the gold atoms found in parts of the sample holder.

Measurements were conducted in air at room temperature, with a gentle flow of helium gas into a 15 mm long pinhole cavity that encapsulates a silicon drift detector, with the exit gas flow located 2 mm from the sample position. The silicon drift detector with an active area of 50 mm^2 was placed in close proximity of the sample to maximize fluorescence photon collection. **Figure 1** shows a schematic of the experiment; the solid angle captured by the detector is $\Omega = 0.04\pi$. The detector not only measures the intensity of the fluorescence photons, but also resolves their energy spectrum, that is, it counts the number of photons reaching the detector as a function of photon energy, as shown in **Figure 2**e. The collected spectrum is then decomposed into the sum of the individual atom-specific spectra with the PyMca software.[22] To determine the atom density from the detected fluorescence, it is compared to an As-containing reference sample from nanoXRF_standards[23] with a known density under the same X-ray beam illumination and placed at the same position as the measured device. The intensity of each fluorescence peak in the spectrum depends not only on the density of atoms participating in the fluorescence process, but also on the ionization cross-section. Note that these X-ray ionization cross-sections are well-known and do not depend on factors such as the atom's depth or environment. In XRF the measured density corresponds to the absolute number of

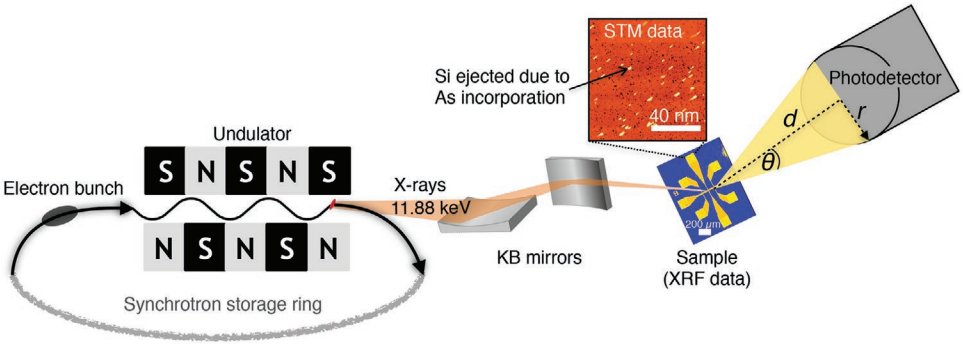

Figure 1. Schematic of the X-ray fluorescence measurement. From left to right: Electron bunches from the synchrotron are directed through the undulator magnets emitting highly collimated photons on account of the repeated electron beam bending. The X-ray beam with a photon energy of 11.88 keV from the synchrotron is focused to 1 μm with the help of a Kirkpatrick-Baez (KB) mirror system. Fluorescence photons from the sample that is illuminated by the X-ray beam are emitted in all directions and a photodetector is placed at $d = 2$ cm away from the sample, collecting the photons from a solid-angle $\Omega = 2\pi(1-\cos\theta) = 2\pi(1-d/\sqrt{d^2+r^2}) = 0.04\pi$. The resulting XRF image (labelled "Sample (XRF data)") shows the As distribution (yellow corresponds to high density). The inset shows an STM height map of the sample's doped Si surface before Si overgrowth; the short bright lines are rows of Si dimers ejected from the surface plane due to the incorporation of As atoms.

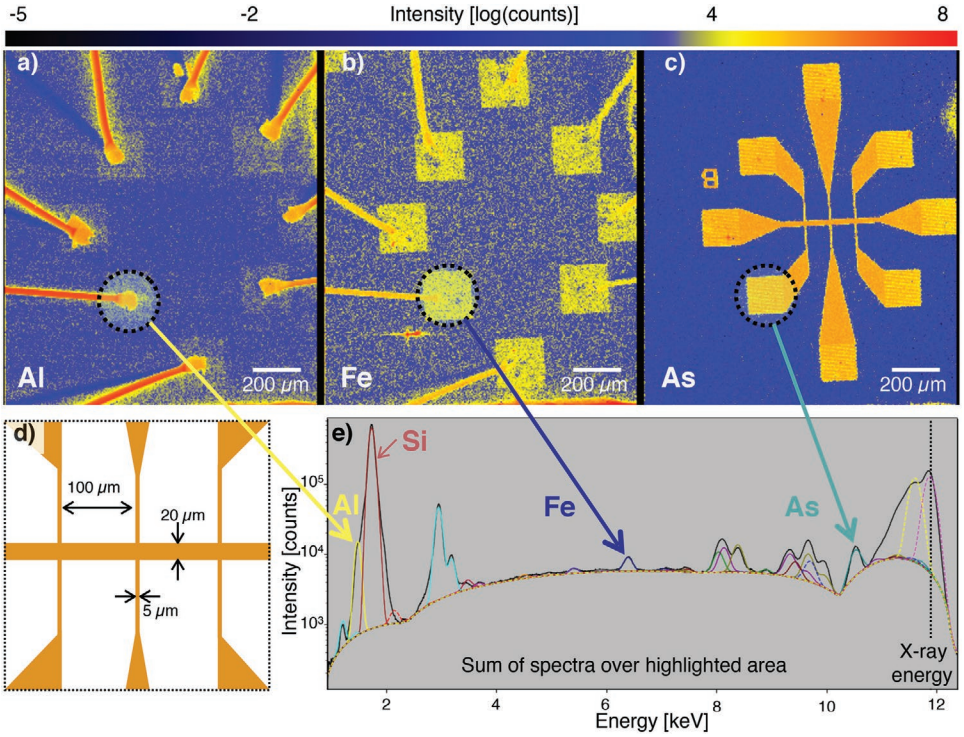

Figure 2. X-ray fluorescence image of an As Hall-bar device. a–c) Al, Fe, and As distribution of device #1 with a density of $n_{As} = 1.4 \times 10^{14}$ cm^{-2} for a photon energy of 11.88 keV, a beam size of 1×1 μm^2, and a step-size of 0.5 μm. At each step a spectrum is recorded during 200 ms. d) Sketch of the top view of the samples with the As Hall-bar structure shown in orange. e) Sum of the fluorescence spectra taken at each scan point within the highlighted area in a)-c). The black line represents the measured data and the colored lines are fits to individual elements. See Figure 5 for details on the elemental contributions.

atoms, unlike other non-destructive imaging techniques which measure only electrically activated dopants.[2] By comparing the atomic density to the free carrier density (obtained from magneto-transport, see Section 4.1) it is thus possible to deduce the activation percentage in a given device. Knowing the dopant electrical activation is important for optimizing device fabrication; in particular when making atomic-scale devices it is crucial to have an activation percentage close to 100% to ensure that all donors contribute an electron to the conduction band.

At the microXAS beamline, the beam position was fixed and the sample swept across the beam with a step size of 500 nm, and for each position a full fluorescence spectrum was recorded. The data collected in this way contain the information of the atomic concentrations at each position of the scan, from all elements that are excited with the chosen X-ray energy. By decomposing the full spectrum at each position into a sum of spectra from each possible element, a 2D elemental density map is obtained.

3. Subsurface Imaging

Structures consisting of atomically thin layers of As ("As δ-layers") buried 30 nm below the Si(100) surface were patterned into 20×200 μm^2 Hall bars and contacted with Al, as detailed in Section 6. The As layer is made by exposing atomically flat Si to a dose of arsine, annealing the wafer to incorporate the As into the surface layers, then overgrowing with epitaxial Si. The As density is simply controlled by the total As dose. Two such structures are studied here, one with a nominal As density of $n_{As} = 1.6 \times 10^{14}$ cm^{-2} and the other with $n_{As} = 1 \times 10^{13}$ cm^{-2}. The dopant density is determined with the STM before the Si overgrowth by counting Si atoms ejected by the incorporated As, as seen in the experimental data shown in the inset of Figure 1 and explained in [24], as well as in Section 6. The same devices were used for the XRF and the magneto-resistance (MR) measurements. **Table 1** summarizes the devices' density and thickness as measured by STM, XRF, SIMS, and MR. Additionally, to quantify the background As dopant density a reference sample was measured. Note that the sample fabrication procedure in this work shares its key steps with hydrogen resist lithography; namely the adsorption and incorporation of dopants on the Si surface, and the subsequent Si deposition. Hence, the maximum dopant concentration and the activation percentage should be identical, as should the dopant position and vertical distribution in the Si lattice. Therefore, conclusions reached here are also valid for devices made with hydrogen lithography.

Figure 2d shows a sketch of the studied devices, where the orange color illustrates the 2D As layer. Figure 2a–c depict the higher density Hall-bar structure #1 as imaged by XRF for Al, Fe, and As, respectively. For each pixel of the image a spectrum is recorded for a duration of 200 ms. The sum of many such spectra is shown in Figure 2e with fitted peaks to deduce the elemental origin. Note that each element's fluorescence spectrum has peaks at unique energies (see Section 6), such

Table 1. Dopant density and layer thicknesses.

Device	n_{STM} (10^{14} cm^{-2})	n_{XRF} (10^{14} cm^{-2})	n_{Hall} (10^{14} cm^{-2})	n_{SIMS} (10^{14} cm^{-2})	t_{SIMS} (nm)	t_{MR} (nm)
#1	1.6 ± 0.3	1.40 ± 0.07	1.31 ± 0.03	1.8 ± 0.2	2.7 ± 0.2	0.97 ± 0.02
#2	0.10 ± 0.03	0.06 ± 0.01	–	0.21 ± 0.02	3.6 ± 0.4	–

The As density n of the two devices measured with STM, XRF, Hall effect, and SIMS. Additionally, the As layer thickness t is given as measured by SIMS and MR. Device #2 was not conductive and, therefore, Hall measurements were not possible.

that fitting the data is straightforward. The ease to distinguish elements is true for arbitrary atomic species. For example, it will be straightforward to discriminate between the various dopants used in hydrogen lithography, such as P [6], As [24], and B [5], making XRF an ideal tool to investigate future multi-dopant-species nano-devices.

The As image in Figure 2c clearly shows the conductive layer of interest, which defines the Hall bar and its contact leads. The unique possibility to distinguish different atomic species makes it possible to verify whether there is contamination in the device. Here the spectrum contains traces of many elements (see Section 6 for element identification), which originate from the lead-less chip-carrier, the glue used to fix the sample, and the He gas that is blown on the sample (traces of Ar in Figure 5). We also see that the Al contact pads and bonding wires contain not only Al, but also a very small quantity of Fe. The exact density is obtained by comparing the intensity of the fluorescence to the reference sample. While the Fe density is only $n_{Fe} = 1 \times 10^{13}$ cm^{-2} in the Al contacts, it provides a stronger XRF signal than the Al whose density is $n_{Al} = 6.0 \times 10^{15}$ cm^{-2}. This is due to the larger (107.3 cm^2 g^{-1}) absorption cross-section of Fe, compared to Al (14.76 cm^{2}g^{-1}), and the considerably larger absorption of the low energy Al fluorescence by the air/He atmosphere and by the detector window. The As density is uniform across the entire Hall bar and is found to be $n_{As} = 1.4 \times 10^{14}$ cm^{-2} and $n_{As} = 5.6 \times 10^{12}$ cm^{-2}, for the two devices measured. For both devices the values obtained with XRF and STM agree within the uncertainty (see Table 1). The uncertainty in XRF measurements is low because atomic cross-sections are universal, such that the use of a reference sample yields an error of less than 5%.

By comparing the atomic density to the free carrier density obtained from Hall measurements we find that the dopant activation in the high-density Hall bar #1 is 94 ± 5%. The low-density device #2 was not conductive and no Hall density could be measured.

The low-density device #2 was also measured in an identical fashion except that the beam size was increased to 1×3 µm^2 yielding a photon flux of $I_0 = 10^{11}$ photons s^{-1}. That way, in the low- and high-density device there were 1.7×10^5 and 1.4×10^6 As atoms within the spot size, respectively. Taking into account the As cross-section, the number of photons absorbed collectively by the As atoms in 200 ms was 1.9×10^5 and 4.8×10^5 photons for the low- and high-density device, respectively. **Figure 3** shows the contrast obtained when measuring the As fluorescence peak intensity across the Hall-bar structures. The contrast in the fluorescence signal when moving the beam on and off the dopant layer has a signal/noise ratio of ≈2 and ≈7 for the low- and high-density device, respectively. Through the use of focusing elements, for example Fresnel zone plates, the X-rays can be focused beyond the beam size of ≈1 µm used here.[25–27] For example in the setup of Döring et al.,[28] a 5 nm spot size is obtained with a flux of 10^9 photons s^{-1}. Considering that for new instruments at next generation synchrotron sources the photon flux will be increased by up to three orders of magnitude,[29] the number of photons absorbed in 200 ms by a single As atom within the 5 nm beam will be about 1.3×10^6, resulting in a similar fluorescence intensity and signal/noise as is seen in our device #1. In this way, it will be possible to obtain XRF images of buried few-atom structures reaching a resolution better than tens of nanometers, thus positioning XRF as an invaluable tool for future quantum- and nano-device inspection.

4. Weak Localization

The XRF images obtained from the 2D As Hall bars show that the technique is highly sensitive and directly discriminates atomic species without requiring any modeling of the

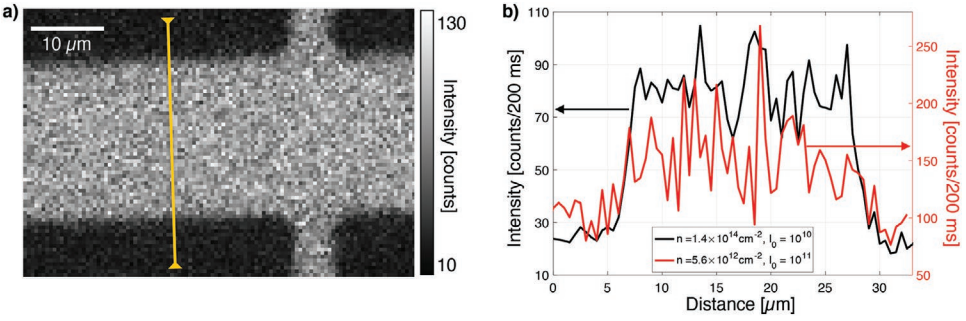

Figure 3. Fluorescence contrast across the Hall bars. a) As fluorescence image of the high-density Hall-bar device #1, taken with a beam size of 1×1 µm^2 and an averaging time of 200 ms. The image is obtained by scanning the sample across the beam, with the x-axis parallel and the y-axis perpendicular to the Hall bar. The yellow line denotes the line trace. b) Line traces in counts per dwell time measured across the Hall bars of the high-density (black, 1×1 µm^2 spot size and photon flux $I_0 = 10^{10}$ photons s^{-1}) and the low-density device (red, 3×1 µm^2 spot size, with 3 µm horizontal width and photon flux $I_0 = 10^{11}$ photons s^{-1}). The As fluorescence signal clearly resolves the 20 µm width of the Hall bar and features a signal/noise ratio of ≈7 and ≈2 for the high- and low-density Hall bars, respectively.

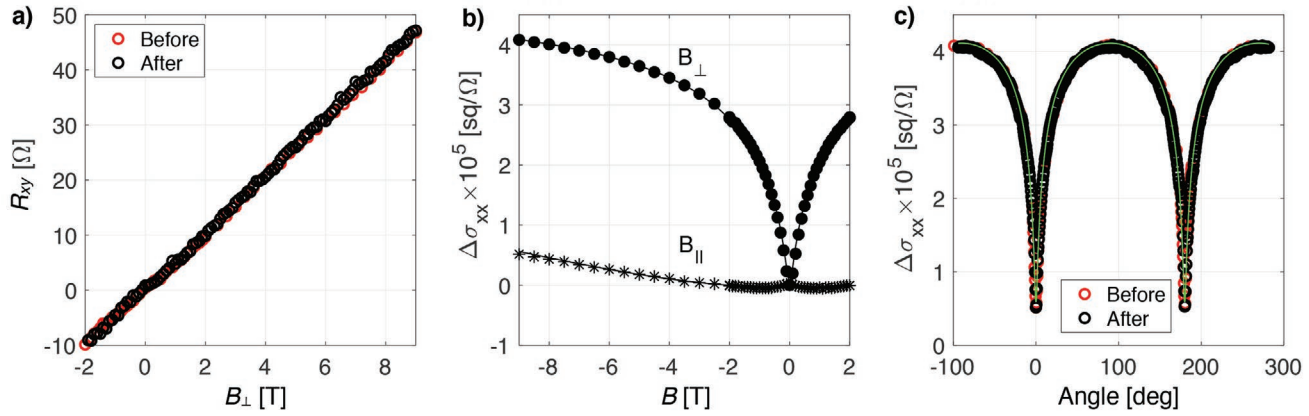

Figure 4. Magneto-transport of the Hall-bar device before and after XRF measurements. a) Hall effect measured at $T = 1.8$ K, before (red) and after (black) the XRF imaging. b) Magneto-conductance for a magnetic field perpendicular (dots) and parallel (stars) to the conductive layer. The lines are fits to equation (1) and (2). c) Change of conductance in square per Ohm, as a function of the magnetic field angle with respect to the conductive layer at an external field of $B = 9$ T (0 ° ≡ in-plane field). The green line is a fit to Equation (4).

sample. An open question concerns the concomitant radiation damage, and to answer this, we measure the low-temperature electrical characteristics of the high-density Hall bar device #1 in magnetic fields up to $B = 9$ T before and after exposure to the X-rays. At $T = 1.8$ K electrons move diffusively, resulting in a conductivity $\sigma_0 > e^2/\hbar$ and are in the so-called weakly localized regime, as evidenced by a logarithmic temperature dependence of the zero-field conductivity.[30–33] Weak localization is a quantum interference effect that occurs for electrons in a medium with time-reversal symmetry, such as silicon, so long as the electrons' coherence length is longer than their mean free path. In that case an electron's trajectory can form a loop and interfere constructively with itself. This interference effect, and particularly its behavior in external magnetic fields, depends strongly on the disorder and dimensions of the electron channel, and so is an ideal diagnostic of radiation damage.

In the weakly localized regime, the conductance can be described by the Hikami-Larkin-Nagaoka theory,[31] in which the conductivity change resulting from an applied magnetic field depends only on the electron mean free path L, the coherence length L_ϕ, and the applied magnetic field B. If the conductive medium is purely 2D and there are no spin-orbit or electron-electron interaction effects, only field components $B_\perp$ perpendicular to the conductive plane can couple to the electrons' orbital degree of freedom. The corresponding conductivity change is then given by

$$\Delta\sigma(B_\perp) = \sigma_0\left[\psi\left(\frac{1}{2}+\frac{B_\phi}{B_\perp}\right) - \psi\left(\frac{1}{2}+\frac{B_L}{B_\perp}\right) + \ln\left(\frac{2L_\phi^2}{L^2}\right)\right] \quad (1)$$

where $\psi(x)$ is the digamma function, $\sigma_0 = \frac{e^2}{2\pi^2\hbar}$, e is the charge of an electron, and $\hbar$ is the reduced Planck constant. The phase-breaking field is given by $B_\phi = \frac{\hbar}{4eL_\phi^2}$ and the elastic characteristic field $B_L = \frac{\hbar}{2eL^2}$.

Our samples have a finite thickness, meaning that electron orbitals can have a small perpendicular component that can couple to a field $B_\parallel$ parallel to the conductive plane, leading to an effect described by[34]

$$\Delta\sigma(B_\parallel) = \sigma_0 \ln(1+\gamma B_\parallel^2) \quad (2)$$

where γ is obtained by fitting the equation to the data and depends on the ∂-layer thickness t and roughness. By fitting $\Delta\sigma(B_\perp)$ and $\Delta\sigma(B_\parallel)$ we can derive this thickness as[35]

$$t = \left(\frac{1}{4\pi}\right)^{1/4}\left[\left(\frac{\hbar}{eL_\phi}\right)^2(\sqrt{n}L\gamma)\right]^{1/2} \quad (3)$$

where n is the free carrier density as measured by the Hall effect. Finally, for tilted magnetic fields the change in conductance can be described by the phenomenological expression[36]

$$\Delta\sigma(B)^p = \Delta\sigma(B_\perp)^p + \Delta\sigma(B_\parallel)^p \quad (4)$$

where p is obtained by fitting the data and is sample and temperature-dependent.

4.1. Magneto-Conductance

To establish whether the XRF imaging technique is non-destructive, we measure the magneto-transport at $T = 1.8$ K of the high-density device #1 before and after the exposure to the X-rays. During the X-ray imaging the sample absorbs 2'000 photons nm^{-2} at an energy of 11.88 keV, corresponding to a radiation dose of 1.5×10^{10} Sv (1.5×10^{16} Rad cm^{-2} or 1.7×10^{-14} J nm^{-3}). Taking into account the absorption lengths of Si and the As atoms doped into Si, as well as the As atom cross-section, we find that each As atom absorbs on average 0.3 photons during the measurement.

Figure 4a shows the Hall effect measured in a magnetic field of up to $B = 9$ T, before and after the X-ray measurement shown in red and black, respectively. The transverse resistance R_{xy} is linear in the field and crosses zero with no signs of quantized,

non-linear, or anomalous Hall effects. Combining the Hall effect with the device's zero-field conductivity gives a mean free path $L = \sqrt{2\pi n}\mu\hbar e = 4.8 \pm 0.1$ nm and L = 4.9 ± 0.2 nm before and after the XRF measurements, respectively, where μ is the electron mobility. The derived Hall electron density is $n = 1.31 \pm 0.03 \times 10^{14}$ cm^{-2} before and $n = 1.27 \pm 0.06 \times 10^{14}$ cm^{-2} after the XRF measurements. As already noted above, comparing the free carrier density to the dopant density obtained from the X-ray fluorescence shows that the activation percentage for this device amounts to 94 ± 5%. Figure 4b shows the magneto-conductance at T = 1.8 K with a field up to B = 9 T applied perpendicular and parallel to the conductive plane. Fitting the data to Equations (1) and (2) yields the electron channel's characteristic parameters. Before the XRF, the magneto-conductance yields a coherence length of L_ϕ = 73.6 ± 0.4 nm and δ-layer thickness of t = 0.98 ± 0.02 nm. After the XRF measurement we obtain L_ϕ = 74.2 ± 0.3 nm and t = 0.97 ± 0.02 nm. Finally, Figure 4c shows the change in conductivity as a function of the out-of-plane angle of a 9 T magnetic field before and after the X-ray measurement. According to Equation (4) the field direction-dependent data contains information of both $\Delta\sigma(B_\perp)$ and $\Delta\sigma(B_\parallel)$. Fitting the data to Equation (4), we obtain $p = 1.9 \pm 0.3$ and $p = 2.3 \pm 0.5$ before and after the XRF, respectively. Combining this with Equations (1) and (2), as well as the Hall measurements implies that, within small error bars, none of the device's electronic characteristics were altered by the X-ray measurement. In particular, it is important to note that the determination of the thickness by the weak-localization measurements has a precision of 0.2 Å, which sets a strict bound to the extent X-rays could have displaced the atoms.

The absence of radiation damage from the X-rays on the As Hall bar can be, as mentioned earlier, transposed to As devices made with hydrogen lithography. As such, XRF is a promising tool for non-invasive inspection of dopant-defined quantum-devices in Si, particularly with the foreseen <10 nm spot size and single dopant sensitivity. The electrical measurements are only sensitive to the activated substitutional donors; as such the non-destructivity conclusion should be valid for any activated As δ-layer fabrication technique, such as molecular-beam epitaxy[37] and ion-implantation.[38] It is also interesting to note that in contrast to ion channeling studies, which showed that high density As donor layers are prone to deactivation upon bombardment with MeV He ions,[39] the use of keV photons for fluorescence does not change the donors' position and activation.

5. Conclusions

We have shown that X-ray fluorescence imaging is a technique well-suited for non-destructive investigation of buried dopant-based devices in Si. This approach has the unique capability of directly identifying dopant species without relying on sample modeling, making it an attractive alternative to bb-EFM and infrared ellipsometry. X-ray scattering techniques can be used in parallel to fluorescence imaging to obtain complementary information, such as strain fields[40] and overall device layout and morphology.[3,4] Additionally, with magneto-transport measurements, we confirm that the technique does not affect the electronic properties of the measured devices, that is, it is non-destructive for As doped Si, an important condition for useful device characterization. This is in contrast to common inspection techniques such as electron microscopy and SIMS which always entail sample destruction. Finally, with the three-orders-of-magnitude enhancements to brilliance expected for next-generation synchrotron beamlines, including focusing optics, as well as improvements both to detector solid angle and signal/noise, it is reasonable to anticipate the ability to locate single As atoms in devices to within several nm over time scales of order seconds per imaging pixel. Radiation effects will then need to be mitigated via the same strategies already exploited for X-ray ptychography today[41,42] and diagnosed exploiting the single electron transistor characteristics of such atoms.[43,44]

6. Experimental Section

Sample Preparation: Si(001) samples were diced to 2 × 9 mm^2 from a 0.5 mm thick, Czochralski-grown wafer, with bulk As doping of density 3×10^{14} cm^{-3}, and resistivity >15 Ω cm. These samples were cleaned ultrasonically in acetone followed by isopropyl alcohol. Each sample was thermally outgassed in vacuum (base pressure $<5 \times 10^{-10}$ mBar) for >8 h at 600 °C, and flash-annealed multiple times at 1200 °C, using direct current resistive sample heating. Sample temperature was monitored using an infrared pyrometer (IMPAC IGA50-LO plus) with a total estimated measurement uncertainty of ± 30 °C.

The samples were dosed with AsH_3 with varying total exposures to control the dopant density. They were then heated at 350 °C for 2 min to incorporate the dopants into the Si lattice.[45] Subsequently, samples were imaged with STM, as shown in Figure 1, and the density of ejected Si atoms was used to estimate the density of incorporated As atoms n_{STM}. All STM measurements were performed in an Omicron variable temperature series STM at room temperature with a base pressure of $<5 \times 10^{-11}$ mBar. After incorporation, 2 nm of Si were deposited on the samples with no resistive sample heating. The samples were then resistively heated to 500 °C for 15 s. This procedure gives a well-confined, electrically active dopant layer.[24,46] A further 28 nm of Si were deposited on the samples held at 250 °C. Si deposition was performed at a base pressure of 2×10^{-10} mBar, using an all-silicon, solid sublimation source (SUSI-40, MBE Komponenten GmbH) operated at a deposition rate of 0.003 nm s^{-1}. During Si deposition, the sample temperature was indirectly monitored by measuring the sample resistance, while heating using a direct current resistive sample heater.

To measure the electrical properties of the dopant layers, the samples were etched into Hall bars. This was done using optical lithography and reactive ion etching. Ohmic contacts were established by deposition of Al into arrays of etched holes extending through the δ-layer.[47] On each sample, two Hall bars were produced, as well as an unetched region to be used for SIMS. The samples were cleaved between the two Hall bars. Each Hall bar was mounted on a chip carrier, and electrically connected to the carrier by Al wire bonds.

X-Ray Fluorescence Spectrum: The fluorescence spectra obtained at each pixel of the XRF images (see Figure 2a-c) are decomposed into a sum of elemental spectra with the help of the PyMca software.[22] An example of a decomposition is presented in **Figure 5**, where the fluorescence spectrum of each separate atomic species is shown. Scattering peaks are also shown as dotted lines; they are the two peaks at highest energy, with the elastic scattering at the incident energy 11.88 keV and the inelastic Compton peak at slightly lower energy. Clearly visible in the spectrum is that each elemental spectrum contains at least one peak at a unique frequency, such that it is straightforward to identify the elements contributing to the spectrum. Only elements that cannot be excited by the incident X-ray energy cannot be detected by fluorescence. For the energy used here, 11.88 keV, the heaviest detectable

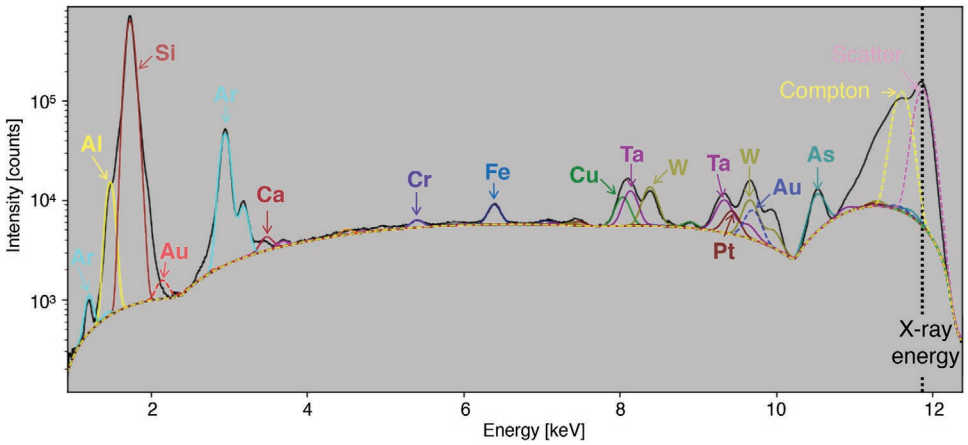

Figure 5. X-ray fluorescence spectrum collected over the highlighted area in Figure 2. The black line represents the data and colored lines are fits to each element's resonant peak. Full lines indicate a *K*-edge, while dotted lines indicate *L* and *M*-edges as well as the scattering peaks.

element is U. To obtain a single element image, as shown in Figure 2a–c, it suffices to isolate the intensity of one elemental fluorescence peak in each pixel at its known energy.

X-Ray Fluorescence Signal/Noise Ratio: To calculate the signal/noise ratio (*SNR*) given in Figure 3, we took two 30 µm traces, one on the doped region (T_{on}) and one off the doped region (T_{off}). The SNR was then simply defined as $SNR = (\text{mean}(T_{On}) - \text{mean}(T_{off}))/\text{std}(T_{On}))$.

Magneto-Transport Setup: For the electrical measurements, a standard Physical Property Measurement System (PPMS) from Quantum Design was used. It contains a cryostat with a superconducting magnet coil, and can control the temperature down to $T = 1.8$ K and the magnetic field up to $B = 9$ T. The samples were bonded on a standard lead-less chip carrier and inserted in a socket attached to a horizontal rotator. The rotator is motor-controlled and the rotation axis is such that the magnetic field can be set from parallel to perpendicular to the current in the Hall bar. The resistance is measured in a four-point geometry using a resistance bridge and with a 5 Hz square-wave 100 nA current. The current is chosen to be in the linear $I - V$ response regime, and such that the Joule heating is negligible.

Secondary-Ion Mass Spectrometry: Time-of-flight SIMS measurements were conducted using an IONTOF ToF-SIMS(5) system with a 25 keV Bi^+ primary ion beam in high current bunch mode, and a 500 eV, 35 nA Cs^+ sputter beam. Depth profiles were made with a 300 × 300 µm^2 sputter crater, and the analytical region was the central 50 × 50 µm^2 of the sputter region. The measured As-ion count rate was converted to a dopant density by measuring a sample of known density with the same setup.

Acknowledgements

The authors thank Jakub Vonka and Manuel Guizar Sicairos for fruitful discussions and technical assistance. The authors acknowledge the Paul Scherrer Institut, Villigen, Switzerland for provision of synchrotron radiation beamtime at the microXAS beamline of the Swiss Light Source. This project received funding from the European Research Council under the European Union's Horizon 2020 Research and Innovation Program, within the Hidden, Entangled and Resonating Order (HERO) project with Grant Agreement 810451. N.D. was partially supported by Swiss National Science Foundation Contract 175867. The authors acknowledge financial support of the Engineering and Physical Sciences Research Council (EPSRC) [Grant Numbers EP/R034540/1, EP/W000520/1]; and Innovate UK [75574]. J.B and P.C.C. were supported by the EPSRC Centre for Doctoral Training in Advanced Characterization of Materials (Grant Number EP/L015277/1), and by the Paul Scherrer Institut. P.C.C. was partially supported by Microsoft.

Conflict of Interest

The authors declare no conflict of interest.

Author Contributions

N.D and G.A. designed the research. N.D, D.F.S., D.G., and G.A. conducted the XRF experiments and analysed the data. J.B., P.C.C., T.J.Z.S., S.F., S.R.S., and N.J.C. fabricated the devices and conducted characterisation measurements at the London Centre for Nanotechnology. N.D, M.B., and Y.S. conducted characterisation measurements at the Paul Scherrer Institut. N.D, G.M., J.B., S.G., and G.A. wrote the manuscript with input from all co-authors.

Data Availability Statement

The data that support the findings of this study are available from the corresponding author upon reasonable request.

Keywords

doped silicon devices, non-destructive sub-surface imaging, X-ray fluorescence

Received: November 10, 2022
Revised: January 17, 2023
Published online:

[1] F. A. Zwanenburg, A. S. Dzurak, A. Morello, M. Y. Simmons, L. C. L. Hollenberg, G. Klimeck, S. Rogge, S. N. Coppersmith, M. A. Eriksson, *Rev. Mod. Phys.* **2013**, *85*, 961.
[2] N. G. Orji, M. Badaroglu, B. M. Barnes, C. Beitia, B. D. Bunday, U. Celano, R. J. Kline, M. Neisser, Y. Obeng, A. E. Vladar, *Nat. Electron.* **2018**, *1*, 532.
[3] M. Holler, M. Odstrcil, M. Guizar-Sicairos, M. Lebugle, E. Müller, S. Finizio, G. Tinti, C. David, J. Zusman, W. Unglaub, O. Bunk, J. Raabe, A. F. J. Levi, G. Aeppli, *Nat. Electron.* **2019**, *2*, 464.
[4] M. Holler, M. Guizar-Sicairos, E. H. R. Tsai, R. Dinapoli, E. Müller, O. Bunk, J. Raabe, G. Aeppli, *Nature* **2017**, *543*, 402.
[5] K. J. Dwyer, S. Baek, A. Farzaneh, M. Dreyer, J. R. Williams, R. E. Butera, *ACS Appl. Mater. Interfaces* **2021**, *13*, 41275.

[6] S. R. Schofield, N. J. Curson, M. Y. Simmons, F. J. Rueß, T. Hallam, L. Oberbeck, R. G. Clark, *Phys. Rev. Lett.* **2003**, *91*, 136104.
[7] K. E. J. Goh, L. Oberbeck, M. Y. Simmons, A. R. Hamilton, M. J. Butcher, *Phys. Rev. B* **2006**, *73*, 035401.
[8] M. Koch, J. G. Keizer, P. Pakkiam, D. Keith, M. G. House, E. Peretz, M. Y. Simmons, *Nat. Nanotechnol.* **2019**, *14*, 137.
[9] F. J. Ruess, L. Oberbeck, M. Y. Simmons, K. E. J. Goh, A. R. Hamilton, T. Hallam, S. R. Schofield, N. J. Curson, R. G. Clark, *Nano Lett.* **2004**, *4*, 1969.
[10] H. Büch, M. Fuechsle, W. Baker, M. G. House, M. Y. Simmons, *Phys. Rev. B* **2015**, *92*, 235309.
[11] V. Brázdová, D. R. Bowler, K. Sinthiptharakoon, P. Studer, A. Rahnejat, N. J. Curson, S. R. Schofield, A. J. Fisher, *Phys. Rev. B* **2017**, *95*, 075408.
[12] B. Voisin, J. Salfi, R. Rahman, S. Rogge, *MRS Bull.* **2021**, *46*, 616.
[13] H. Werner, P. Boudewijn, *Vacuum* **1984**, *34*, 83.
[14] A. S. Chang, L. J. Lauhon, *Curr. Opin. Solid State Mater. Sci.* **2018**, *22*, 171.
[15] E. Zschech, A. Diebold, *AIP Conf. Proc.* **2011**, *1395*, 233.
[16] G. Gramse, A. Kölker, T. Škereň, T. J. Z. Stock, G. Aeppli, F. Kienberger, A. Fuhrer, N. J. Curson, *Nat. Electron.* **2020**, *3*, 531.
[17] A. M. Katzenmeyer, T. S. Luk, E. Bussmann, S. Young, E. M. Anderson, M. T. Marshall, J. A. Ohlhausen, P. Kotula, P. Lu, D. M. Campbell, T.-M. Lu, P. Q. Liu, D. R. Ward, S. Misra, *J. Mater. Res.* **2020**, *35*, 2098.
[18] M. D. de Jonge, C. Holzner, S. B. Baines, B. S. Twining, K. Ignatyev, J. Diaz, D. L. Howard, D. Legnini, A. Miceli, I. McNulty, C. J. Jacobsen, S. Harteveld, *Proc. Natl. Acad. Sci.* **2010**, *107*, 15676.
[19] A. S. Schulz, C. A. M. Harteveld, G. J. Vancso, J. Huskens, P. Cloetens, W. L. Vos, *ACS Nano* **2022**, *16*, 3674.
[20] F. Adams, B. Vekemans, G. Silversmit, B. De Samber, L. Vincze, in *Microscopic X-ray Fluorescence Analysis with Synchrotron Radiation Sources*, Springer, Boston, MA **2011**, pp. 1737–1759.
[21] D. Grolimund, A. Scheidegger, J. van der Veen, R. Abela, *PSI Sci. Rep.* **2002**, *4*, 139.
[22] V. Solé, E. Papillon, M. Cotte, P. Walter, J. Susini, *Spectrochim. Acta Part B: Atom. Spectrosc.* **2007**, *62*, 63.
[23] http://www.nanoxrf.com/?page_id=106 (accessed: August 2022).
[24] T. J. Z. Stock, O. Warschkow, P. C. Constantinou, J. Li, S. Fearn, E. Crane, E. V. S. Hofmann, A. Kölker, D. R. McKenzie, S. R. Schofield, N. J. Curson, *ACS Nano* **2020**, *14*, 3316.
[25] F. Villar, L. Andre, R. Baker, S. Bohic, J. C. da Silva, C. Guilloud, O. Hignette, J. Meyer, A. Pacureanu, M. Perez, M. Salome, P. van der Linden, Y. Yang, P. Cloetens, *Synchrotron Rad. News* **2018**, *31*, 9.
[26] J. Park, Y. Ahn, J. A. Tilka, K. C. Sampson, D. E. Savage, J. R. Prance, C. B. Simmons, M. G. Lagally, S. N. Coppersmith, M. A. Eriksson, M. V. Holt, P. G. Evans, *APL Mater.* **2016**, *4*, 066102.
[27] A. Troian, G. Otnes, X. Zeng, L. Chayanun, V. Dagytė, S. Hammarberg, D. Salomon, R. Timm, A. Mikkelsen, M. T. Borgström, J. Wallentin, *Nano Lett.* **2018**, *18*, 6461.
[28] F. Döring, A. Robisch, C. Eberl, M. Osterhoff, A. Ruhlandt, T. Liese, F. Schlenkrich, S. Hoffmann, M. Bartels, T. Salditt, H. Krebs, *Opt. Express* **2013**, *21*, 19311.
[29] H. Braun, T. Garvey, M. Jörg, A. Ashton, P. Willmott, R. Kobler, ... E. Zehnder, *Paul Scherrer Institut* **2021**, PSI Bericht Report No.: 21-02.
[30] P. A. Lee, T. V. Ramakrishnan, *Rev. Mod. Phys.* **1985**, *57*, 287.
[31] S. Hikami, A. I. Larkin, Y. Nagaoka, *Prog. Theor. Phys.* **1980**, *63*, 707.
[32] B. Altshuler, A. Aronov, in *Electron–Electron Interactions in Disordered Systems*, (Eds.: A. Efros, M. Pollak), Modern Problems in Condensed Matter Sciences, Vol. *10*, Elsevier, Amsterdam **1985**, pp. 1–153, https://www.sciencedirect.com/science/article/pii/B9780444869166500077.
[33] R. G. Wheeler, *Phys. Rev. B* **1981**, *24*, 4645.
[34] P. M. Mensz, R. G. Wheeler, *Phys. Rev. B* **1987**, *35*, 2844.
[35] D. F. Sullivan, B. E. Kane, P. E. Thompson, *Appl. Phys. Lett.* **2004**, *85*, 6362.
[36] G. Matmon, E. Ginossar, B. J. Villis, A. Kölker, T. Lim, H. Solanki, S. R. Schofield, N. J. Curson, J. Li, B. N. Murdin, A. J. Fisher, G. Aeppli, *Phys. Rev. B* **2018**, *97*, 155306.
[37] O. D. Dubon, P. G. Evans, J. F. Chervinsky, M. J. Aziz, F. Spaepen, J. A. Golovchenko, M. F. Chisholm, D. A. Muller, *Appl. Phys. Lett.* **2001**, *78*, 1505.
[38] L. Eriksson, J. A. Davies, N. G. E. Johansson, J. W. Mayer, *J. Appl. Phys.* **1969**, *40*, 842.
[39] J. Haskell, E. Rimini, J. W. Mayer, *J. Appl. Phys.* **1972**, *43*, 3425.
[40] T. U. Schülli, S. J. Leake, *Curr. Opin. Solid State Mater. Sci.* **2018**, *22*, 188.
[41] M. Odstrcil, M. Holler, J. Raabe, A. Sepe, X. Sheng, S. Vignolini, C. G. Schroer, M. Guizar-Sicairos, *Nat. Commun.* **2019**, *10*, 2600.
[42] J. Deng, Y. Yao, Y. Jiang, S. Chen, T. M. Mooney, J. A. Klug, F. S. Marin, C. Roehrig, K. Yue, C. Preissner, Z. Cai, B. Lai, S. Vogt, *Opt. Express* **2022**, *30*, 26027.
[43] X. Wang, J. Wyrick, R. V. Kashid, P. Namboodiri, S. W. Schmucker, A. Murphy, M. D. Stewart, R. M. Silver, *Commun. Phys.* **2020**, *3*, 82.
[44] M. Fuechsle, J. A. Miwa, S. Mahapatra, H. Ryu, S. Lee, O. Warschkow, L. C. L. Hollenberg, G. Klimeck, M. Y. Simmons, *Nat. Nanotechnol.* **2012**, *7*, 242.
[45] K. E. J. Goh, L. Oberbeck, M. Y. Simmons, *Phys. Status Solidi A* **2005**, *202*, 1002.
[46] J. G. Keizer, S. Koelling, P. M. Koenraad, M. Y. Simmons, *ACS Nano* **2015**, *9*, 12537.
[47] M. M. Fuechsle, Ph.D. Thesis, UNSW Sydney, **2011**.